Aerospace Science and Technology 119 (2021) 107207

Contents lists available at ScienceDirect

Aerospace Science and Technology

www.elsevier.com/locate/aescte

# IDDES method based on differential Reynolds-stress model and its application in bluff body turbulent flows

Gang Wang [a], Quanzheng Li [a], Yi Liu [b,*]

[a] School of Aeronautics, Northwestern Polytechnical University, Xi'an, 710072, China
[b] LNM, Institute of Mechanics, Chinese Academy of Sciences, Beijing, 100190, China

ARTICLE INFO

*Article history:*
Received 8 July 2021
Received in revised form 18 September 2021
Accepted 5 November 2021
Available online 12 November 2021
Communicated by Cummings Russell

*Keywords:*
Detached-eddy simulation
Reynolds-stress model
Massively separated flows
Tandem cylinders
Launch vehicle
Transonic buffet

ABSTRACT

A general construction approach for a class of detached-eddy simulation (DES) methods with the turbulent length-scale equation is presented in this study. It supports the rationality of the construction and provides a theoretical estimation of the model coefficients in DES simulation. By using the construction approach, a differential Reynolds-stress model (RSM), referred to as Speziale-Sarkar-Gatski (SSG)/Launder–Reece–Rodi (LRR)-$\omega$ RSM, is built into the improved delayed DES (IDDES) method. After calibration of the model parameters in the IDDES method and basic validation for decaying isotropic turbulence, the RSM-based IDDES approach is then applied to simulate the massively separated flows around the tandem cylinders and the transonic buffet flow over a hammerhead launch vehicle. The simulations are validated by the available experimental data, and the performance is evaluated by means of instantaneous, statistical, spectral analysis of the numerical data. It is found that the RSM-based IDDES method shows better performance comparing with the k-$\omega$ shear-stress transport (SST)-based IDDES method, especially for predicting the development of massively separated flows behind the bluff body.



## 1. Introduction

Flows around the bluff bodies are widespread in the engineering applications [1], such as the flow past an aircraft, a spacecraft, or an express train. Normally, the flow behind the bluff body undergoes periodic vortex shedding, causing structural vibrations, acoustic noise [2], and significant increases in the mean drag and lift fluctuations. In particular, when the object is located in the wake of a bluff body, for example, the vertical tail in the wake of the wing [3], the booster behind the payload fairing of the rocket [4], and the slat inner surface of multi-element airfoil [5], etc., buffeting will occur due to the vortex shedding from the bluff body. Considering the above-mentioned flow phenomena, various measures such as noise reduction, optimization of lift and drag characteristics, and accurate prediction of buffeting are widely concerned in engineering. The studies on the flow past the bluff body have high engineering application value. Moreover, for the flows at high Reynolds number (Re), the bluff wake is almost a massively separated turbulent flow with the generation and evolution of various scale vortex structures. Therefore, it is challenging to simulate in detail and is often used to test the potential of turbulence models.

In the industrial community, the hybrid Reynolds-averaged Navier-Stokes/large eddy simulation (RANS/LES) methods are considered promising in massive separation flows at high Re due to the high efficiency of the RANS combined with the fine resolution of the LES. Several hybrid RANS/LES strategies were suggested, which includes the partially averaged Navier-Stokes method (PANS) [6], the partially integrated transport model (PITM) [7], the detached-eddy simulation (DES) [8], the zonal detached-eddy simulation (ZDES) [9], etc., where the DES-type method is the most widely known. In the last two decades, noticeable progress has been reached in building the DES-type method thanks to the joint efforts of many scholars and researchers [10]. The DES-type methods and its variant of delayed DES (DDES) [11], improved delayed DES (IDDES) [12], and extended DDES [13], have become increasingly popular in the industrial community [14]. The original concept of DES presented by Spalart et al. in 1997 was based on the Spalart–Allmaras (SA) one-equation turbulence model [8]. Inspired by the success of Spalart, some other RANS turbulence models were built into the DES methods. Strelets [15] proposed another DES, which is based on the k-$\omega$ shear-stress transport (SST) model. Xiao [16] applied the weakly nonlinear k–$\omega$ turbulence model to the DDES method. Solkeun [17] also developed a DES method based on the k-$\varepsilon$-v2-f turbulence model. The capability of these DES methods and their variants has been demonstrated in many test cases. Some representative works are as follows. Xiao and

* Corresponding author.
*E-mail address:* liuyi@imech.ac.cn (Y. Liu).

https://doi.org/10.1016/j.ast.2021.107207
1270-9638/

Zhang [18] have assessed the performance of the SST-based IDDES (SST-IDDES) in simulating both attached and separated flows. The results showed a good agreement with experiments, and the "grey area" was alleviated by using the shear-layer-adapted subgrid length scale. Chen [19] used the SA-based DDES method (SA-DDES) to investigate the massively separated flow around the tandem cylinders. The results showed a good agreement with experiments. Liu and Wang [20] performed SA-DDES in simulations around a hammerhead launch vehicle to investigate the flow mechanism of the hammerhead configuration during transonic buffeting, and the features of buffet flow reported in the experiment have been reproduced. Mirzaei and Sohankar [21] have evaluated the capacity of the k-$\omega$-v2-f-based DDES method on the plane channel flow, wavy channel flow, and two side-by-side square cylinders. A good agreement between the results of the DDES and the LES was obtained for all flow configurations employed. He and Liu [22] proposed a dynamic DDES method to study the wall heat transfer in impinging jets. In their study, the DDES model was improved by dynamically computing the model coefficients. The mean and fluctuating velocity fields are reasonably captured. These works apply various RANS models to the DES method, thereby rapidly promoting the development of the DES method. In addition, the extensive applications of the DES method in massively separation flows have contributed to the verification and validation of the DES method.

Mockett [23] pointed out that the sensitivity of DES to the underlying RANS model cannot be negligible for separation flow and elucidated the importance of RANS modeling in a DES context. However, most DES-type methods are based on the one-equation model or two-equation model that invoke the eddy-viscosity assumption for modeling the Reynolds stress. Therefore, a DES based on the model other than the one-equation model or two-equation model is desirable to provide a simulation method for "problem" flow where eddy viscosity model may fail to predict separation accurately. The Reynolds-stress model (RSM) is the most elaborate type of RANS turbulence model. Abandoning the isotropic eddy-viscosity hypothesis, the RSM closes the Reynolds-averaged Navier-Stokes equations by solving transport equations for the Reynolds stress. Recently, some RANS simulation studies [24–27] have shown that the RSM model is better than the eddy viscosity model in accounting for more detailed representation of the flow physics, such as the effects of streamline curvature and rapid changes in strain rate, etc. To investigate the potential of the RSM model in the hybrid RANS/LES method for separated flows, a few recent studies have been conducted. Probst and Radespiel [28] applied the $\varepsilon^{h}$-RSM [29] model to the DDES method to simulate the flow over the backward-facing step and the HGR-01 airfoil. Zhuchkov and Utkina [30] used the enhanced DES [31] method based on the Speziale-Sarkar-Gatski (SSG)/Launder–Reece–Rodi (LRR)-$\omega$ RSM [32] model to simulate the flow over the axisymmetric SMC000 nozzle. The RSM-based DES-type method presented by Probst is based on the $\varepsilon^{h}$-RSM model which is suitable for the low Reynolds number flows, and the DES-type method presented by Zhuchkov is based on enhanced DES which is normally used for jet flow simulation. The need for accuracy of the RANS model in DES is no less than in pure RANS, and some studies [33–35] have shown that the SSG/LRR-$\omega$ RSM model performs well in the simulation of high Reynolds number flows. In addition, since the IDDES method can avoid Grid Induced Separation (GIS) and Logarithmic Layers Mismatched (LLM) problems to a certain extent, it is more adaptable to the complex bluff body configurations. Therefore, considering the strong requirement of simulating flow around a bluff body with the high Reynolds number in engineering, the SSG/LRR-$\omega$ RSM model is applied to the IDDES method (RSM-IDDES) by a relatively general DES construction approach in this study.

In this work, we have proposed a novel construction approach that provides an idea for the introduction of a large class of RANS models to the DES method. It supports the rationality of the construction and presents a theoretical estimation of the DES parameters $C_{DES}$ to provide a reference for its calibration. By using the construction approach, a RSM-based IDDES method has been built and implemented in an in-house code. The decaying isotropic turbulence (DIT) flow is used to calibrate the RSM-IDDES method presented here, and tandem cylinders and a transonic hammerhead launch vehicle are simulated to validate the RSM-IDDES method. The arrangement of the paper is as follows. In Section 2, the numerical methods and the turbulence modeling including the SSG/LRR-$\omega$ RSM model and the construction approach of DES are presented. Furthermore, the calibration and validation of the RSM-IDDES method are given in Section 3. In Section 3.1, the parameter $C_{DES}$ is calibrated through the DIT flow. In Section 3.2 and 3.3, the simulation results of two configurations obtained by the RSM-IDDES method are presented and discussed. The RSM-IDDES method is validated by comparing the results with available experimental data. Its ability for simulating the massively separated flows around the bluff body is examined by comparing the results with the SST-IDDES simulations. Finally, several concluding remarks are given in the last section.

## 2. Turbulence modeling and numerical methods

### 2.1. Numerical methods

In the present work, an in-house CFD solver HUNS3D [36], which has the functionality of simulating both steady and unsteady viscous flows, is used as the baseline flow solver. In the HUNS3D flow solver, the fluid motion is governed by the time-dependent Navier-Stokes equations for the ideal gas, which are expressed by the conservation of mass, momentum, and energy for the compressible fluid with the absence of external forces. The equations expressed in integral form for a bounded domain $\Omega$ with boundary $\partial\Omega$ are given below.

$$\frac{\partial}{\partial t}\iiint_{\Omega}\boldsymbol{Q}\,d\Omega+\iint_{\partial\Omega}\boldsymbol{F}(\boldsymbol{Q})\cdot\boldsymbol{n}ds=\iint_{\partial\Omega}\boldsymbol{G}(\boldsymbol{Q})\cdot\boldsymbol{n}ds+\iint_{\partial\Omega}\boldsymbol{G}_{turb}(\boldsymbol{Q})\cdot\boldsymbol{n}ds \tag{1}$$

Where, $\boldsymbol{Q}=[\rho,\rho u,\rho v,\rho w,\rho E]^T$, $\boldsymbol{F}(\boldsymbol{Q})\cdot\boldsymbol{n}ds$ and $\boldsymbol{G}(\boldsymbol{Q})\cdot\boldsymbol{n}ds$ respectively represent convective and viscous flux terms (further details are given in Ref. [36]). $\boldsymbol{G}_{turb}(\boldsymbol{Q})\cdot\boldsymbol{n}ds$ represents turbulent viscous flux contributed by the Reynolds stress on the RANS branch, and the subgrid-scale stress on the LES branch. The governing equations are discretized with the cell-centered finite volume method on unstructured hybrid meshes composed of hexahedrons, prisms, tetrahedrons, and pyramids. The discretized convective flux term is computed with the second-order Roe discretization scheme, and the discretized viscous flux term is obtained by the reconstructed central scheme. For the Roe scheme, the modulus of the eigenvalues is modified using Harten's entropy correction [37], and the second-order accuracy is achieved by reconstructing the solution following Barth's interpolation method [38]. The LU-SGS relaxation-based implicit backward-Euler scheme is implemented for steady flow simulation and the corresponding second-order full implicit dual time scheme is adopted for unsteady flow case. An adaptive local time-stepping method was developed to eliminate the adverse influence of some poor-quality grids on solution stability and convergence speed. In addition, a form of locally adaptive flux blending [39,40] has been implemented in the Roe scheme,

ensuring the dominance of low dissipation in the LES region and more stability in the RANS region. The details of the adaptive dissipation Roe scheme are listed in Appendix A.

### 2.2. SSG/LRR-ω Reynolds-stress model

The SSG/LRR-$\omega$ RSM model [24], developed by the DLR, is a combination of the Speziale–Sarkar–Gatski model and the Launder-Reece-Rodi model. It directly solves for the Reynolds stress $\overline{\rho}\tilde{R}_{ij} = \overline{\rho u_i'' u_j''}$. Here the hat represents the Favre average and $\overline{\rho}$ is the Reynolds-averaged density. The Reynolds stress transport equation is given by

$$\frac{\partial}{\partial t}(\overline{\rho}\tilde{R}_{ij}) + \frac{\partial}{\partial x_k}(\overline{\rho}\tilde{U}_k\tilde{R}_{ij}) = \overline{\rho}P_{ij} + \overline{\rho}\Pi_{ij} - \overline{\rho}\varepsilon_{ij} + \overline{\rho}D_{ij} + \overline{\rho}M_{ij} \tag{2}$$

Where the production term $\overline{\rho}P_{ij}$ is calculated by average quantities exactly

$$\overline{\rho}P_{ij} = -[\tilde{U}_{i,k}\overline{\rho}\tilde{R}_{kj} + \tilde{U}_{j,k}\overline{\rho}\tilde{R}_{ki}] \tag{3}$$

Where the $\tilde{U}_{i,k}$ denotes the gradient of mean velocity $\tilde{U}_{i,k} = \frac{\partial \tilde{U}_i}{\partial x_k}$. The dissipation $\overline{\rho}\varepsilon_{ij}$ is modeled by an isotropic tensor with the components

$$\overline{\rho}\varepsilon_{ij} = \frac{2}{3}\overline{\rho}\varepsilon\delta_{ij} \tag{4}$$

All other terms on the right-hand side of Eq. (2) require modeling. The details of these terms are not shown here and could be found in Ref. [24]. To close the Reynolds stress transport equations, an additional turbulent length-scale transport equation is required for providing a measure of the isotropic dissipation rate $\varepsilon$. The SSG/LRR-$\omega$ model follows Menter's approach, and the so-called baseline (BSL) $\omega$ equation is used to estimate $\varepsilon$ ($\varepsilon = C_\mu \tilde{k}\omega$, where $\tilde{k} = \overline{\rho u_k'' u_k''}/2\overline{\rho}$ is turbulent kinetic energy (TKE), $C_\mu = 0.09$). It reads as follows:

$$\begin{aligned}&\frac{\partial}{\partial t}(\overline{\rho}\omega) + \frac{\partial}{\partial x_k}(\overline{\rho}\tilde{U}_k\omega)\\ &= \overline{\rho}P^{(\omega)} + \overline{\rho}D^{(\omega)} + \frac{\partial}{\partial x_k}\left[\left(\overline{\mu} + \sigma_\omega\frac{\overline{\rho}\tilde{k}}{\omega}\right)\frac{\partial\omega}{\partial x_k}\right] + \overline{\rho}C_D\end{aligned} \tag{5}$$

The details of the terms and constants in Eq. (5) are also provided in Ref. [24]. The numerical solution of the turbulence equation (2) and Eq. (5) is similar to the mainstream equation (1) except that its convective flux adopts the first-order Roe scheme.

### 2.3. The construction approach of DES-type method

The key point of the hybrid RANS/LES method is how to bridge the RANS and LES methodologies. For the DES-type method, the establishment of the bridge is mostly based on the RANS turbulence equation with certain modifications to obtain a subgrid-scale simulation in the LES region. Due to the above characteristics of the DES-type method, the subgrid-scale quantities in the LES region of the DES-type method all adopt the corresponding turbulence model equations as their transport equations except for the modified terms. Usually, the Smagorinsky subgrid-scale stress model, which is a simple and widely used model, is assumed in the LES region. Since the underlying RANS equation is generally a differential equation, it cannot strictly satisfy the Smagorinsky subgrid model in the LES region for most flows, but holds only in some special cases. Apply the equilibrium assumption in the following derivation, the assumption is also adopted into the SA-based and SST-based DES-type method [8,15]. The Smagorinsky subgrid-scale stress model reads as follows.

$$\upsilon_t = (C_S\Delta)^2|\widetilde{S}_{ij}| \tag{6}$$

Where $\upsilon_t$ is the subgrid-scale eddy viscosity, $C_S$ is the Smagorinsky coefficient (recommended value is 0.18), $\Delta$ is the grid length scale which is proportional to the implicit filter scale, and $|\widetilde{S}_{ij}| = \sqrt{2\widetilde{S}_{ij}\widetilde{S}_{ij}}$ denotes the modulus of average strain rate tensor. By a simple dimensional analysis, $\upsilon_t$ can be expressed as $\upsilon_t = \ell\mathcal{V}$, where $\mathcal{V}$ is the subgrid-scale velocity scale and $\ell$ is the subgrid length scale. $\mathcal{V}$ is usually taken as the square root of subgrid-scale kinetic energy $\sqrt{\tilde{k}}$. Considering the incompressible turbulence and under the assumption of Boussinesq eddy viscosity, the subgrid-scale stress is expressed as $R_{ij}^{SGS} = 2\overline{\rho}\upsilon_t\widetilde{S}_{ij} - (2/3)\overline{\rho}\tilde{k}\delta_{ij}$. The following equation can be obtained by the double-dot product of strain rate tensor and subgrid stress.

$$R_{ij}^{SGS}\widetilde{S}_{ij} = \overline{\rho}\upsilon_t|\widetilde{S}_{ij}|^2 - (2/3)\overline{\rho}\tilde{k}\widetilde{S}_{ii} \tag{7}$$

Eq. (7) can be further simplified by the definition of strain rate tensor ($\widetilde{S}_{ij} = (\tilde{U}_{i,j} + \tilde{U}_{j,i})/2$).

$$R_{ij}^{SGS}\tilde{U}_{i,j} = \overline{\rho}\upsilon_t|\widetilde{S}_{ij}|^2 \tag{8}$$

And then, Eq. (9) can be obtained by $\upsilon_t = \ell\mathcal{V}$ and Eq. (6)

$$\overline{\rho}(\ell\sqrt{\tilde{k}})^3/(C_S\Delta)^4 = R_{ij}^{SGS}\tilde{U}_{i,j} \tag{9}$$

In fact, $R_{ij}^{SGS}\tilde{U}_{i,j}$ in Eq. (9) is equal to the production of subgrid-scale kinetic energy $\tilde{k}$. Therefore, under the assumption of equilibrium turbulence which means that the production is equal to the dissipation, the expression of subgrid-scale kinetic energy dissipation $\overline{\rho}\varepsilon$ can be obtained from Eq. (9).

$$\overline{\rho}\varepsilon = \overline{\rho}(\ell\sqrt{\tilde{k}})^3/(C_S\Delta)^4 \tag{10}$$

$\ell$ is the subgrid length scale that depends on the turbulent length-scale variable $\phi$ (e.g., $\varepsilon$, $\omega$, etc.) which is taken to close the equation and further defined as $\ell = C_\ell\tilde{k}^{\frac{m}{n}+\frac{3}{2}}\phi^{-\frac{1}{n}}$. Where $C_\ell$ is a scale factor, m and n respectively depend on the definition of $\phi$ which is mostly written as $\phi = C_\mu^{-1}\tilde{k}^m\varepsilon^n$. E.g., for k-$\omega$ turbulence model, those parameters are specified as $\phi = \omega$, $m = -1$, $n = 1$, $C_\mu = 0.09$, and $C_\ell = 1$; For k-$\varepsilon$ turbulence model, those parameters are specified as $\phi = \varepsilon$, $m = 0$, $n = 1$, $C_\mu = 1$, and $C_\ell = 0.09$. In fact, $\ell$ is proportional to the grid scale $\Delta$, a rigorous proof will be given and the expression of proportional factor related to DES parameter $C_{DES}$ will also be determined below. The transport equation of turbulence variable $\phi$ is mostly obtained from the k-equation and $\varepsilon$-equation.

$$\frac{D\phi}{Dt} = m\frac{\phi}{\tilde{k}}\frac{D\tilde{k}}{Dt} + n\frac{\phi}{\varepsilon}\frac{D\varepsilon}{Dt} \tag{11}$$

Where the operator D represents the material derivative. According to Ref. [41], in homogeneous turbulence, the k-equation and $\varepsilon$-equation can be simplified to $\frac{D\tilde{k}}{Dt} = \upsilon_t|\widetilde{S}_{ij}|^2 - \varepsilon$ and $\frac{D\varepsilon}{Dt} = C_{\varepsilon 1}\frac{\varepsilon}{\tilde{k}}\upsilon_t|\widetilde{S}_{ij}|^2 - C_{\varepsilon 2}\frac{\varepsilon^2}{\tilde{k}}$ respectively. Then, substituting the above two equations into Eq. (11), the transport equation of turbulence variable $\phi$ can be expressed as

$$\frac{D\phi}{Dt} = C_{\phi 1}\frac{\phi}{\tilde{k}}\upsilon_t|\widetilde{S}_{ij}|^2 - C_{\phi 2}\frac{\phi}{\tilde{k}}\varepsilon \tag{12}$$

Where $C_{\phi 1}$ and $C_{\phi 2}$ are model factors of $\phi$-equation. It is necessary to explain that $C_{\phi 1} = m + nC_{\varepsilon 1}$ and $C_{\phi 2} = m + nC_{\varepsilon 2}$, where $C_{\varepsilon 1}$ and $C_{\varepsilon 2}$ are the model factors of $\varepsilon$-equation, for the standard $\phi$-equation (11). But there is a certain difference between actual model factors and values calculated from the previous two equations since the actual $\phi$-equation is obtained by modifying or discarding certain terms in Eq. (11). Furthermore, in equilibrium turbulence, Eq. (12) can be simplified to $C_{\phi 1}\upsilon_t|\widetilde{S}_{ij}|^2 = C_{\phi 2}\varepsilon$. Where, the $\varepsilon$ is obtained from the length scale definition $\ell = C_{\ell\varepsilon}\tilde{k}^{\frac{3}{2}}\varepsilon^{-1}$ and the eddy viscosity coefficient expression $\upsilon_t = \sqrt{\tilde{k}}\ell$. That is $\varepsilon = C_{\ell\varepsilon}\upsilon_t^3/\ell^4$. Then the following equation can be obtained

$$\upsilon_t = \sqrt{C_{\phi 1}/(C_{\ell\varepsilon}C_{\phi 2})}\ell^2|\widetilde{S}_{ij}| \tag{13}$$

Where $C_{\ell\varepsilon} = 0.09$ is $C_\ell$ of $\varepsilon$. Thus, the proposition that $\ell$ is proportional to $\Delta$ is confirmed by comparing with Eq. (6).

$$\ell = \left[C_{\phi 1}/(C_{\ell\varepsilon}C_{\phi 2})\right]^{-1/4} C_S\Delta \tag{14}$$

Substituting Eq. (14) into Eq. (10), the subgrid-scale kinetic energy dissipation can be expressed as

$$\overline{\rho}\varepsilon = \overline{\rho}\tilde{k}^{1.5}/\left[C_S\left[C_{\phi 1}/(C_{\ell\varepsilon}C_{\phi 2})\right]^{3/4}\Delta\right] \tag{15}$$

The coefficient of $\Delta$ is denoted by $C_{DES}$, and then $C_{DES}\Delta$ is denoted by $l_{LES}$. Considering that $\overline{\rho}\varepsilon$ returns to the original model in the RANS region, $l_{RANS}$ is defined as $(1/C_\mu^{1/n}C_\ell)\ell$. Then the bridge between RANS and LES is established by the turbulent kinetic energy dissipation, which ensures that the original model is returned in the RANS region and the Smagorinsky subgrid-scale stress model is obtained under the assumption of equilibrium turbulence in the LES region.

$$\overline{\rho}\varepsilon = \begin{cases} \textit{LES region:} \\ \dfrac{\overline{\rho}\tilde{k}^{1.5}}{l_{LES}} = \dfrac{\overline{\rho}\tilde{k}^{1.5}}{C_{DES}\Delta}, \qquad C_{DES} = C_S\left[C_{\phi 1}/(C_{\ell\varepsilon}C_{\phi 2})\right]^{3/4} \\ \textit{RANS region:} \\ \dfrac{\overline{\rho}\tilde{k}^{1.5}}{l_{RANS}} = \dfrac{\overline{\rho}\tilde{k}^{1.5}}{(1/C_\mu^{1/n}C_\ell)\ell}, \qquad \ell = C_\ell\tilde{k}^{\frac{m}{n}+\frac{3}{2}}\phi^{-\frac{1}{n}} \end{cases} \tag{16}$$

Eq. (16) presents the construction approach, which only needs to modify the dissipation of turbulent kinetic energy with Eq. (16), for a large class of DES methods (the turbulent length-scale equation is contained in turbulence model) and the theoretical estimation of the DES parameter $C_{DES}$. However, in numerical simulation, $C_{DES}$ is different from the theoretical value due to numerical dissipation. Therefore, the theoretical estimation of $C_{DES}$ only provides a reference, and the basic turbulent flow (e.g., decaying isotropic turbulence) is required for $C_{DES}$ calibration in actual applications. It can be obtained from Eq. (16) that the value of $C_{DES}$ indirectly affects the Smagorinsky coefficient $C_S$ in the LES region, so the dynamic determination of $C_{DES}$ can obtain a dynamic Smagorinsky model in the LES region of DES simulation. He and Liu [42] presented the dynamic SST-DDES method, and applied it to the simulation of periodic hills and impinging jet. The dynamic SST-DDES method achieved a better performance than the original SST-DDES method.

For the k-$\omega$ SST-based DES-type model, the turbulent length-scale variable is defined as $\phi = \omega$, therefore $m = -1$, $n = 1$, $C_\mu = 0.09$ and $C_\ell = 1$. Therefore, the RANS length scale can be constructed from Eq. (16) as

$$l_{RANS} = \sqrt{\tilde{k}}/(C_\mu\omega) \tag{17}$$

And the LES length scale as $l_{LES} = C_{DES}\Delta$, where $C_{DES}$ is obtained by the weighted average of $C_{DES,k-\omega}$ and $C_{DES,k-\varepsilon}$ through the Menter's blending function $F_1$ [43].

$$C_{DES} = F_1 C_{DES,k-\varpi} + (1 - F_1)C_{DES,k-\varepsilon} \tag{18}$$

The theoretical estimation of $C_{DES,k-\omega}$ is 0.805 ($C_S = 0.18$, $C_{\phi 1} = 0.55$, $C_{\phi 2} = 0.83$) and $C_{DES,k-\varepsilon}$ is 0.630 ($C_S = 0.18$, $C_{\phi 1} = 0.44$, $C_{\phi 2} = 0.92$), with calibration values of 0.78 and 0.61, respectively.

For the SSG/LRR-$\omega$ RSM DES-type model, the dissipation term of Reynolds stress Eq. (4) is modified by Eq. (16). The RANS length scale in Eq. (16) is also defined by Eq. (17) due to the turbulent length-scale equation of SSG/LRR-$\omega$ RSM model is the same as k-$\omega$ SST model. The turbulent kinetic energy $\tilde{k}$ in Eq. (17) is obtained with half trace of Reynolds stress tensor.

$$\tilde{k} = R_{ii}/2 \tag{19}$$

The LES length scale defined as $l_{LES} = C_{DES}\Delta$, where $C_{DES}$ is similar with SST based DES-type method that is obtained by the weighted average of $C_{DES,LRR}$ and $C_{DES,SSG}$ through $F_1$. The theoretical estimation of $C_{DES,LRR}$ and $C_{DES,SSG}$ in SSG/LRR-$\omega$ RSM-DES type model is the same as the k-$\omega$ SST-DES type model $C_{DES,SSG} = 0.630$ and $C_{DES,LRR} = 0.805$, since the theoretical estimation of $C_{DES}$ is only related to some coefficients in the length-scale equation and Smagorinsky coefficient $C_S$. Additionally, the $C_{DES}$ of RSM-DES type model in actual applications is calibrated in Section 3.1.

### 2.4. Improved delayed DES (IDDES) method

In the previous section, only the formulation of the model in the RANS region and LES region was presented, but the conversion rule between the two regions was not given. For the DES method, the conversion mechanism is seamless and automatic, which switches the length scale of the RANS and LES regions automatically by introducing a mixing length in the dissipation term, e.g., k-$\omega$ SST-DES: $\overline{\rho}\varepsilon = \overline{\rho}\tilde{k}^{1.5}/l_{DES}$; SSG/LRR-$\omega$ RSM-DES: $\overline{\rho}\varepsilon_{ij} = \frac{2}{3}(\overline{\rho}\tilde{k}^{1.5}/l_{DES})\delta_{ij}$. The definition of the mixing length is determined by different DES-type methods (e.g., DES97, DDES, IDDES, etc.). The IDDES method is selected in this study as it avoids GIS and LLM problems to a certain extent. The IDDES mixing length is given by

$$l_{IDDES} = \overline{f}_d(1 + f_e)l_{RANS} + (1 - \overline{f}_d)l_{LES} \tag{20}$$

Where $l_{RANS}$ and $l_{LES}$ were defined in the previous section, respectively, and the definition of blending function $\overline{f}_d$, elevating function $f_e$ in Eq. (20) are given in Ref. [12]. In addition, the grid scale of IDDES is redefined as $\Delta = \min[\max(C_w d, C_w\Delta_{\max}, d_{wn}), \Delta_{\max}]$. Where $C_w$ is an empirical constant (recommended value is 0.15), and d is the distance to the wall, $d_{wn}$ is the grid step in the wall-normal direction, and $\Delta_{\max}$ is defined as the maximum local grid spacing $\Delta_{\max} = \max(\Delta x, \Delta y, \Delta z)$.

## 3. Results and discussions

### 3.1. Decay of isotropic turbulence (DIT)

The first case in this section is dedicated to the calibration of the computational procedure for the DES model, whereby the results for the RSM-IDDES variant are shown and discussed. Constant values calibrated form the basis for all further results obtained in this section. This calibration process is considered as an essential prerequisite for a DES computation. Decaying isotropic turbulence (DIT) represents the simplest realization of turbulent flow and is therefore a fundamental test case for the new turbulence modeling. For this purpose, DIT computations are conducted with various

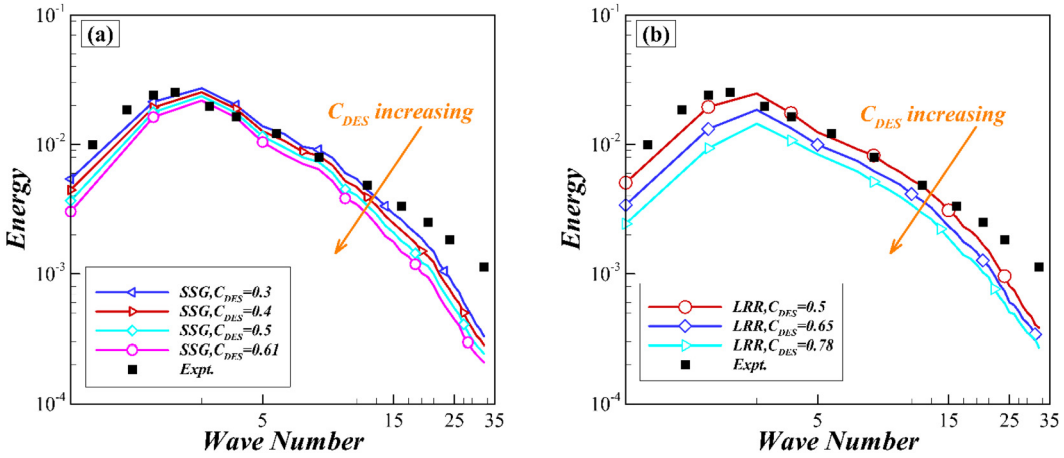


**Fig. 1.** Effect of different $C_{DES}$-constants in RSM-IDDES on the energy spectrum in the DIT case, $t^* = 2.0$ (a. SSG branch, b. LRR branch).

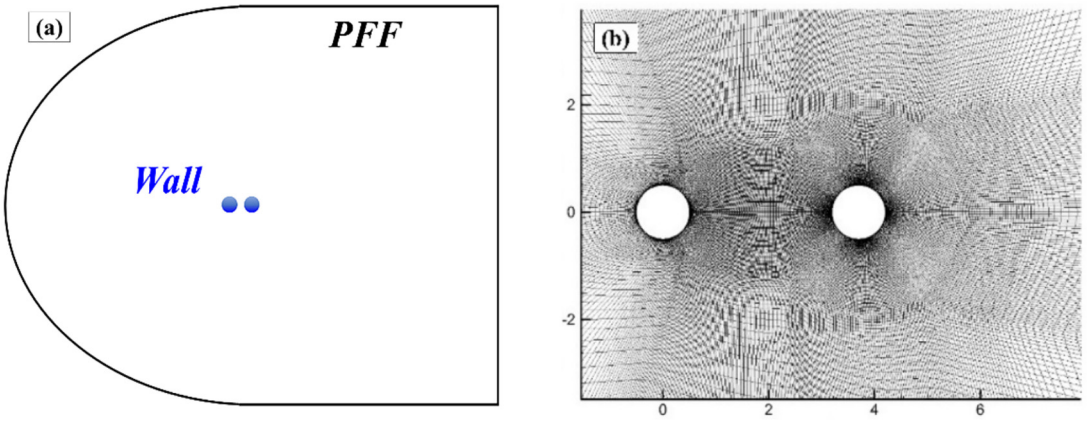


**Fig. 2.** Baseline computational grid for tandem cylinder configuration (a: the boundary conditions, b: the grid near the wall).

values for $C_{DES}$. The grid employed consists of $64^3$ rectangular and equidistant control volumes. The physical domain is a rectangular box of edge length $2\pi$ for which the lowest and highest resolved wavenumbers are therefore 1 and N/2, respectively. Since the flow over tandem cylinders and payload fairing are conducted with the adaptive dissipation Roe scheme, the calibration of $C_{DES}$ is also performed with this scheme. The formulation of the adaptive dissipation Roe scheme is given in Appendix A. We have also performed the DIT simulations with the Roe scheme. The results are shown in Appendix B.

Simulations of DIT are performed in a cubic computational domain with three pairs of periodic boundary conditions in each spatial direction. The second-order full implicit dual time-stepping scheme is adopted, with time step of 0.001 non-dimensional units for each case. The velocity field for the solution initialization was obtained from inverse Fourier transform of the experimental spectra presented by Comte-Bellot and Corrsin [44], which is referred to as CBC data in many studies. The underlying RANS model in current DES methods contains SSG and LRR branches, and the final $C_{DES}$ is blended by the function F1. Therefore, $C_{DES}$ can be calibrated separately. The calibration process mainly requires two elements, the initial value of the calibration and the variation trend of the energy spectrum with the change of $C_{DES}$. First, the analysis in Section 2.3 shows that the theoretical estimation of $C_{DES}$ for RSM-IDDES is equal to SST-IDDES, so the initial calibration values of $C_{DES,SSG}$ and $C_{DES,LRR}$ are taken as the values of $C_{DES,k-\varepsilon}$ and $C_{DES,k-\omega}$ calibrated by Menter as, $C_{DES,k-\varepsilon} = 0.61$ and $C_{DES,k-\omega} = 0.78$. In addition, considering the relationship between the Smagorinsky constant $C_S$ and the Kolmogorov constant $C_K$ ($C_S \approx C_\Delta^{-1}(1.5C_K)^{-3/4}$ [45]) and Eq. (16), it can be seen that $C_{DES}$ should be reduced when the energy intercept of inertial zone energy spectrum ($\ln C_K + (2/3)\ln\varepsilon$, Kolmogorov's 1941 theory) is smaller than the experimental value during the calibration process, and vice versa. Fig. 1 shows the resulting normalized energy spectra over the normalized wavenumber for different $C_{DES}$ values at $t^* = 2.0 (t^* = t \cdot V_\infty / L_{ref.})$. Results obtained from $C_{DES,SSG} = 0.3$ and $C_{DES,LRR} = 0.5$ agree well with the measured spectra. Other values yield too much dissipation in the small turbulent scales.

### 3.2. Tandem cylinders

The second case is the flow past a tandem cylinder configuration (L=3.7D) at Ma=0.1285 and $Re_D = 1.6 \times 10^5$. Experimental data presented by Jenkins [46] and Neuhart et al. [47] is used to assess the performance of the RSM-IDDES method. This case was known to associate with the complex flow, such as the separation of turbulent boundary layer, free shear layer instability [48], the interaction of unsteady wake of the front cylinder with the downstream one [49], and unsteady flow with massive separation between cylinders [50], and so on. It is also the standard test case in the European Seventh Framework Project Advanced Turbulence Simulation for Aerodynamic Application Challenges project (ATAAC) [51]. The computational grid is obtained by extending the two-dimensional grid provided by ATAAC (as shown in Fig. 2b), which is widely used in the simulation of the tandem cylinders [52–54]. The counts of cells in the two-dimensional domain are 92,500 and 120 layers are arranged in the spanwise direction, resulting in 11.1 million cells in total. Computations are conducted

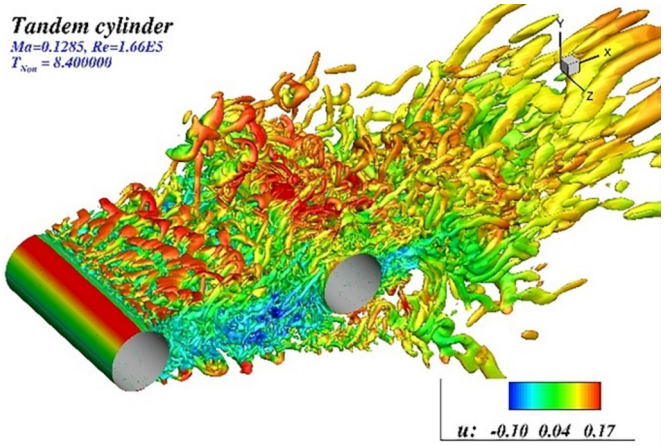


**Fig. 3.** Iso-surfaces of the Q-criterion colored with the velocity magnitude ($Q = 0.5(\Omega_{ij}\Omega_{ij} - S_{ij}S_{ij})$, $Q_{iso} = 0.5$). (For interpretation of the colors in the figures, the reader is referred to the web version of this article.)

with pressure far field (PFF) and no-slip wall conditions, as well as periodic conditions applied in the spanwise direction.

The turbulent structures of the flow are illustrated by plotting iso-surfaces of the Q-invariant ($Q = 0.5(\Omega_{ij}\Omega_{ij} - S_{ij}S_{ij})$), where $\Omega_{ij}$ and $S_{ij}$ denote the antisymmetric and symmetric components of $\nabla u$, respectively. Fig. 3 shows the iso-surfaces of the Q-criterion ($Q_{iso} = 0.5$) obtained by applying the RSM-IDDES method to the flow past a tandem cylinder configuration. The complex nature of the flow arising from this configuration is clearly observed. The vortex shedding and development are well captured by RSM-IDDES. A sequence of vortexes rolling up in the shear layer from the front cylinder is being convected downstream that grows in size and ultimately impinges on the rear cylinder.

The distributions of mean pressure coefficient Cp for the upstream and downstream cylinder are compared with the experiment in Fig. 4. It shows that the mean Cp distributions on both cylinders are almost identical and in good agreement with the experimental measurements. The root-mean-square (RMS) pressure coefficient for both cylinders is compared with the experiment in Fig. 5. On the upstream cylinder, the peaks associated with flow separation are well predicted. On the downstream cylinder, the *Cprms* peaks located at 45° to 315° represent the vortex impingement from the upstream cylinder. It is observed that these peak values are slightly overpredicted by the SST-IDDES method. The results obtained by the RSM-IDDES method show better agreement with the experiment. Besides, on the downstream cylinder, the overall curve and flow separation (i.e., at $\theta \approx 110^O$ and $250^O$) obtained from RSM-IDDES are in better agreement with the experimental measurements. Fig. 6 compares the instantaneous spanwise vorticity contours in the mid-section plane predicted by both the SST-IDDES method and the RSM-IDDES method. The experimental data extracted from PIV measurements are also shown for comparison. In order to compare with the experimental result, the instantaneous flow fields at the same time are extracted. The time is determined at the instantaneous that the flow topology by simulations is the most similar with that of experiment. The SST-IDDES method predicts a delayed onset of shear layer instability, while RSM-IDDES predicts a shorter shear layer and more small-scale structures similar to the measurement.

The power spectral densities (PSD) of the surface pressure at different angles $\theta$ on the upstream and downstream cylinders are shown in Fig. 7. The primary vortex shedding frequency and the corresponding magnitudes are listed in Table 1. It shows that the frequency of the fluctuating pressure at sample A is similar to sample B. Compared with experimental data (180 Hz), the primary vortex shedding frequency is picked up better by RSM-IDDES (176 Hz), compared with the frequency provided by SST-IDDES is 172 Hz. The magnitude of the pressure fluctuation is captured well by both DDES within 1.8% error margin.

### 3.3. Hammerhead launch vehicle configuration

The basic geometry used in this investigation was the Model 11 hammerhead launch vehicle configuration (hereby mentioned as hammerhead configuration) from NASA report [55]. It is a simple axisymmetric launch vehicle shape with a payload section larger than the second-stage diameter. Experimental investigations were conducted by Ames research centers. The computational conditions selected correspond to the wind tunnel test conditions. The Mach number is Ma=0.81, the Reynolds number based on the diameter of the first stage booster ($D_{ref} = 12$ *inches*) is $\mathrm{Re} = 4.2 \times 10^6$ and the angle of attack (AOA) is set as 0 degrees. An O–H topology grid (as shown in Fig. 8a) is generated for numerical calculation, the first layer spacing was chosen using the approach of Cummings et al. [56], such that the average $y^+ < 0.5$, the growth rate in the boundary layer is 1.21. To reduce the amount of computational grid, symmetric boundary condition, as shown in Fig. 8b, is applied to the half-model calculation. The detailed grid division refers to Ref. [20], which has discussed the grid sensitivity, and further refinement is performed here based on the high-density grid in Ref. [20]. The grid is locally refined in the separation and shock motion areas, particularly, close to the payload section to properly model the shear layer instability, as shown in Fig. 8a. In detail, the azimuthal direction grid in the refined zone starting from the top of the fairing cylinder as shown in Fig. 8a is 140 points and the streamwise direction grid is 470 points. The total cell counts are approximately 18.5 million. The unsteady time step is 0.01, which is nondimensionalized by the sound speed of free-stream and unit one meter. SST-IDDES simulation with the same grid and settings is performed for comparison.

Fig. 9a shows the instantaneous contour of the density gradient on the cross-section through the generatrix of the hammerhead configuration obtained by RSM-IDDES and SST-IDDES. The evolution process of the free shear layer is illustrated from Fig. 9a. It develops from the extending boundary layer of the trailing edge of the fairing cylinder and gradually loses stability after a period of extension. After the free shear layer loses stability (known as the Kelvin–Helmholtz instability process, termed by K-H instability), it breaks into various scales vortices and finally strikes on the second stage of the hammerhead configuration. Additionally, it can also be roughly seen that the shear layer instability simulated by the RSM-IDDES method is earlier than SST-IDDES, and the vortex structures after breaking are smaller. Fig. 10 shows the subgrid stress distribution calculated by the two models, and it can be seen that the components of the subgrid stress calculated by the RSM-IDDES method are all smaller than those obtained by the SST-IDDES method in each region (shear layer extension region, shear layer broken region). For shear layer extension region, according to the views presented by Spalart in Ref. [31], the smaller subgrid stress calculated by the RSM-IDDES method is beneficial to unlock the occurrence of K-H instability, thereby speeding up the instability of the shear layer. In the separation bubble, the smaller subgrid stress means that the modeled turbulence energy by RSM-IDDES is smaller such that a finer vortex structure is resolved. Fig. 9b displays the iso-surfaces of the Q-criterion obtained by applying the RSM-IDDES method to the hammerhead configuration, displaying the evolution process of the vortex structures flowing through the hammerhead configuration. The flow around the hammerhead configuration can be regarded as an axisymmetric back-step flow [57], and a series of quasi-two-dimensional toroidal vortices are rolled up after the trailing edge of the fairing cylinder, which is similar to the two-dimensional backward-facing step flow. With the oc-

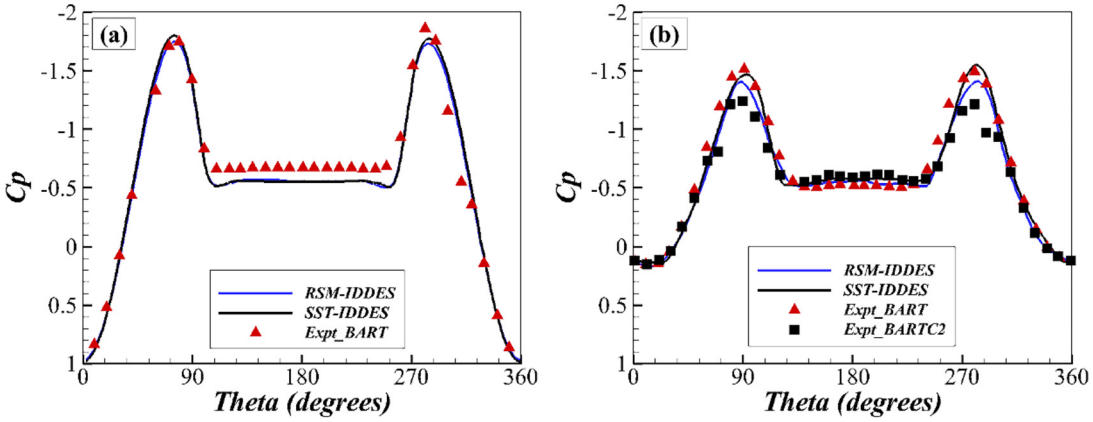


**Fig. 4.** Mean pressure coefficients on the tandem cylinder surfaces compared with experiment (a: upstream, b: downstream).

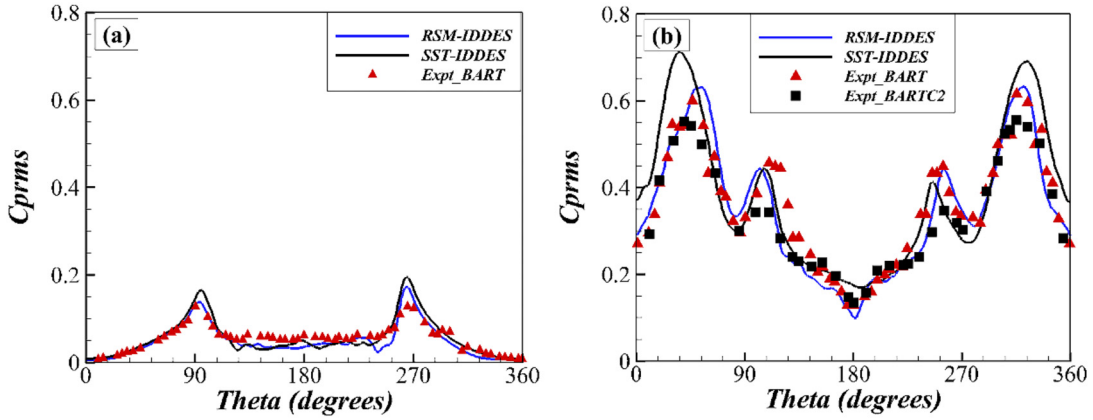


**Fig. 5.** The RMS of pressure coefficients on the tandem cylinder surfaces compared with experiment (a: upstream, b: downstream).

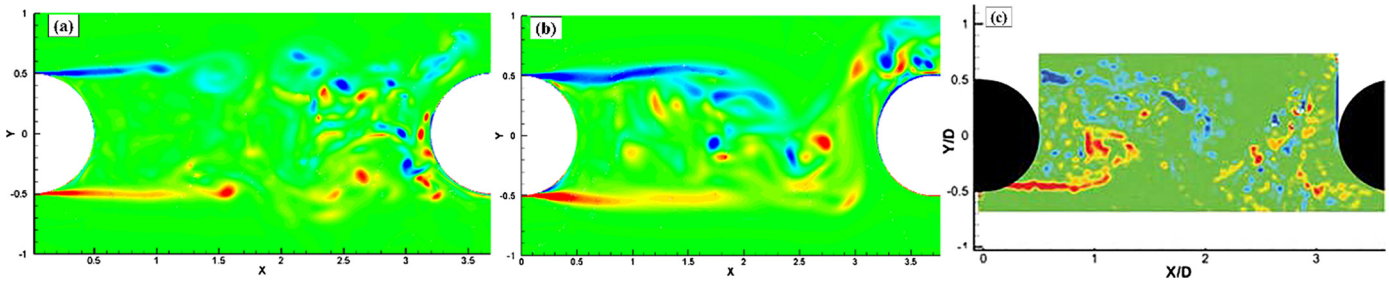


**Fig. 6.** Contours of instantaneous spanwise vorticity in the mid-section plane (a: RSM-IDDES, b: SST-IDDES, c: experiment).

**Table 1**
Primary frequency and the corresponding SPL predicted by different methods.

| Item | Frequency at A, Hz | SPL at sample A, dB | Frequency at B, Hz | SPL at sample B, dB |
|---|---|---|---|---|
| SST-IDDES | 172 | 115.6 | 172 | 137.6 |
| RSM-IDDES | 176 | 114.3 | 176 | 136.8 |
| Experiment | 179 | 116.5 | 180 | 138.6 |

currence of K-H instability, the toroidal vortices gradually bend, break, pair, and ultimately impinge on the second stage. In the reattachment zone, the vortices gradually evolve into the hairpin-like structure and longitudinal vortices.

The computed $Cp_{avg}$ (averaged pressure) and $Cp_{rms}$ (root-mean-square of fluctuation pressure) distributions of the two models are plotted with experimental data in Fig. 11. The experimental data presented by Coe and Nute was band-pass filtered (10-800 Hz). Therefore, to compare with the experimental data, the computed $Cp_{avg}$ and $Cp_{rms}$ in Fig. 11 are also filtered. The comparison between the experimental data and computed $Cp_{avg}$ is plotted in Fig. 11a. As can be seen from the figure, the results of the two models are both in good agreement with the experimental data, especially the RSM-IDDES method is more consistent than the SST-IDDES method in the recirculation region downstream of the faring boat tail, $0.35<x<0.65$. Fig. 12a intuitively shows the discrepancy between the two models in $Cp_{avg}$ from the perspective of the spatial mean flow regime. It can be seen from the figure that the

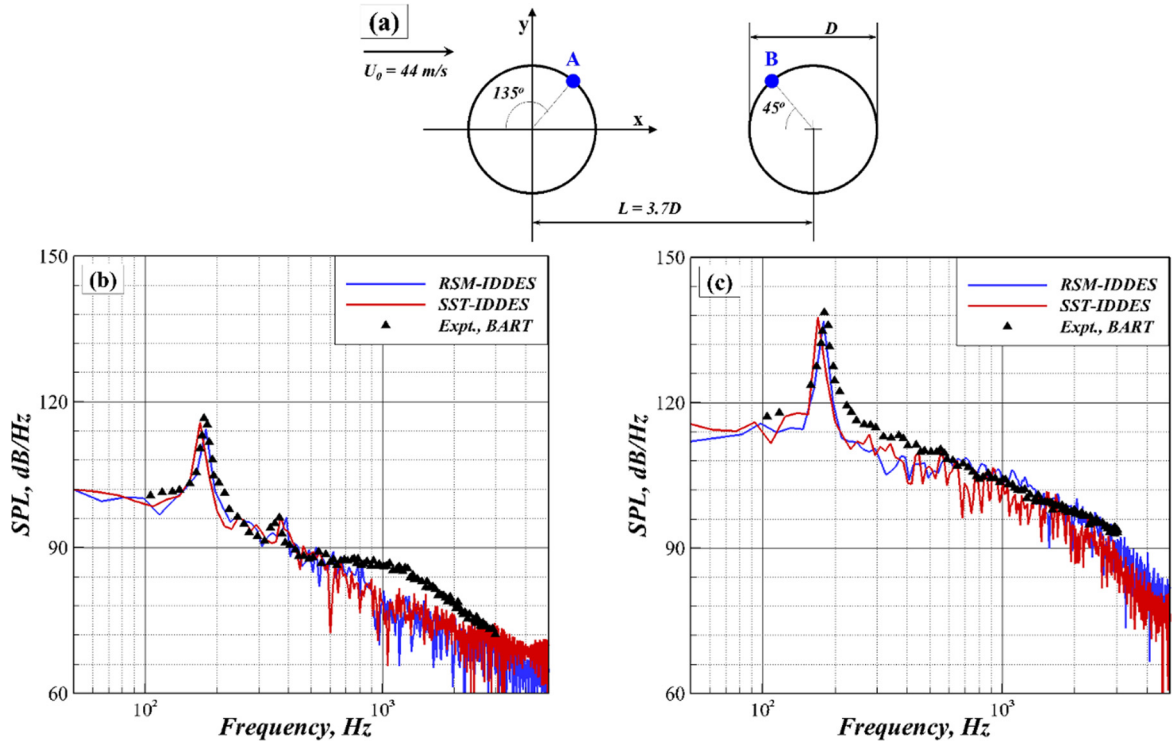


**Fig. 7.** PSD of pressure at A and B (a: the location of A and B, b: PSD of pressure at A, c: PSD of pressure at B).

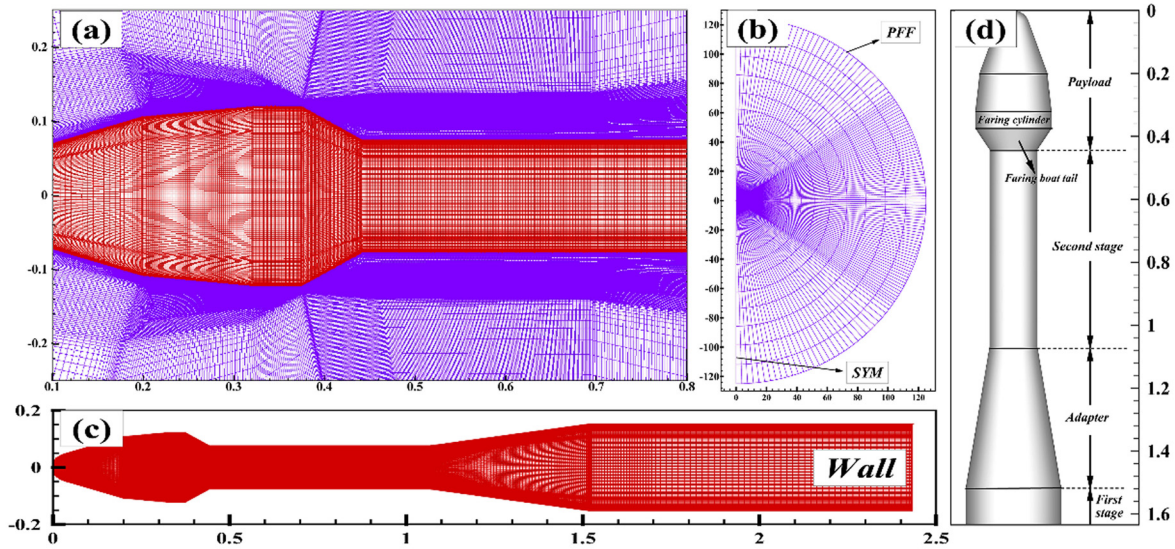


**Fig. 8.** Computational grid for half-body configuration: (a) Topology of the grid in the vicinity of the payload faring. (b) The Far field and symmetric boundary conditions. (c) Surface grids in a side view. (d) Part names of hammerhead launch vehicle configuration.

streamline flowing out of the trailing edge of the fairing cylinder gradually bends away from the main flow and finally attaches to the second stage of the hammerhead configuration forming a separation bubble. The flow in the separation bubble is recirculated from the attachment point to upstream. As illustrated from the contour of the wall friction coefficient, in the recirculation zone, there is a section of the attached flow which corresponds to the increasing section, $0.5<x<0.7$, of $Cp_{avg}$ in Fig. 11a. And then the flow separates from the wall surface as the recirculation flow gradually approaches the faring boat tail. The size of the separation bubble formed by the impact of the free shear layer on the wall affects the position of the reattachment zone, which in turn affects $Cp_{avg}$ distribution.

The comparison between the experimental data and computed $Cp_{rms}$ is plotted in Fig. 11b. First, considering the peak position of $Cp_{rms}$, the position can be estimated at x=0.58 from the experimental data, which are mostly consistent with the result calculated by the RSM-IDDES method, but there is some discrepancy when calculated with SST-IDDES method and the position is near x=0.62. The discrepancy of $Cp_{rms}$ on the wall can be explained by the spatial distribution. Fig. 12b shows the distribution of $Cp_{rms}$ on the cross-section along the generatrix and the wall surface calculated by the two models. Considering Fig. 9a, the mechanism for distribution of $Cp_{rms}$ in Fig. 12b can be analyzed. After the free shear layer flowing out from the trailing edge of the fairing cylinder has undergone an extension process, it begins to lose stability

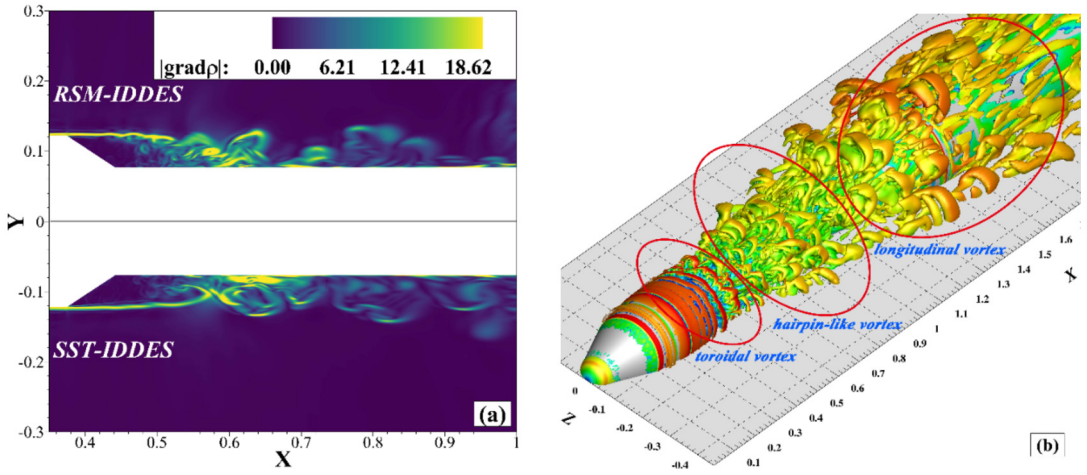


**Fig. 9.** a: Instantaneous density gradient contour obtained from SST-IDDES and RSM-IDDES; b: Iso-surface of Q-criterion obtained by the RSM-IDDES simulation at Ma=0.81.

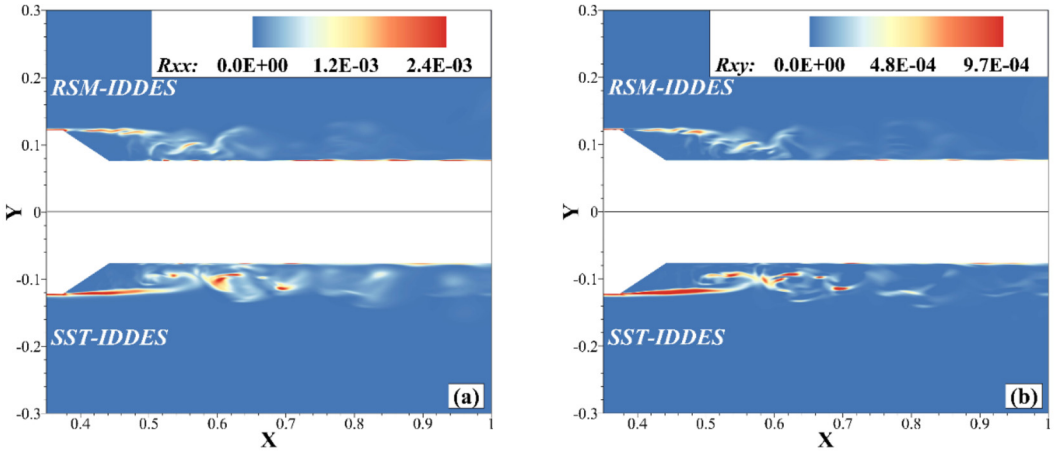


**Fig. 10.** The instantaneous subgrid stress contour obtained from SST-IDDES and RSM-IDDES (a. the normal stress; b. the shear stress).

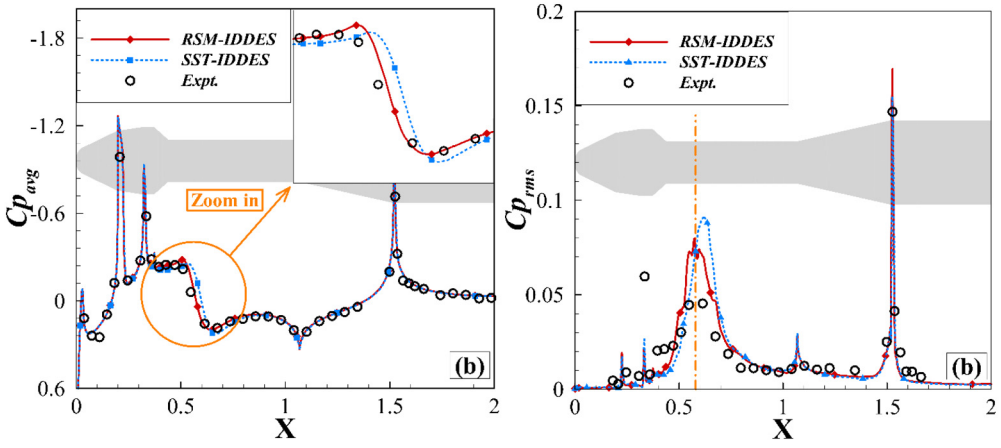


**Fig. 11.** $Cp_{avg}$ and $Cp_{rms}$ distribution obtained by SST-IDDES and RSM-IDDES (a: $Cp_{avg}$, b: $Cp_{rms}$).

gradually at a certain point in the flow field and produces the fluctuation pressure. As the instability and breaking process of the free shear layer continues, a region containing various scales vortices that have significant fluctuation pressure is formed, furthermore this region intersects with the wall surface, forming a ring-shaped fluctuation pressure distribution on the surface. The position of the ring-shaped region is related to the peak position of $Cp_{rms}$, meanwhile it is affected by the speed of the instability process of the free shear layer under the mean sense. Because the instability process predicted by the RSM-IDDES method is faster than SST-IDDES (the arrows in Fig. 12b indicate the previous statement on average, besides the instantaneous situation is shown in Fig. 9a), the peak position of $Cp_{rms}$ by RSM-IDDES method is more forward than SST-IDDES method. Fig. 13 shows the time averaged subgrid stress calculated by the two methods, which reflects the instability process of the free shear layer under the mean sense. The red ribbon

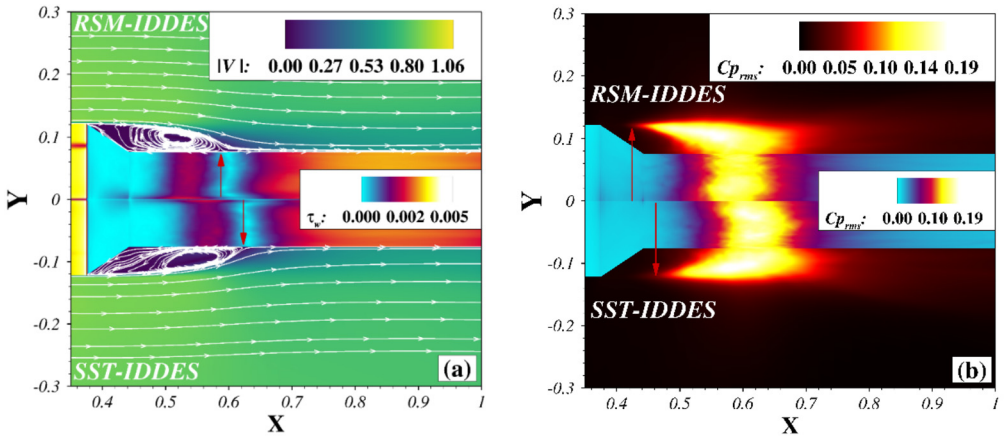


**Fig. 12.** a: Mean flow field contour obtained from SST-IDDES and RSM-IDDES, fluid zone is colored by mean velocity (nondimensionalized by the speed of sound) and filled with mean streamlines and surface zone is colored by the mean friction coefficient; b: Mean fluctuation flow field contour obtained from SST-IDDES and RSM-IDDES, colored by the root mean square of fluctuation pressure coefficient.

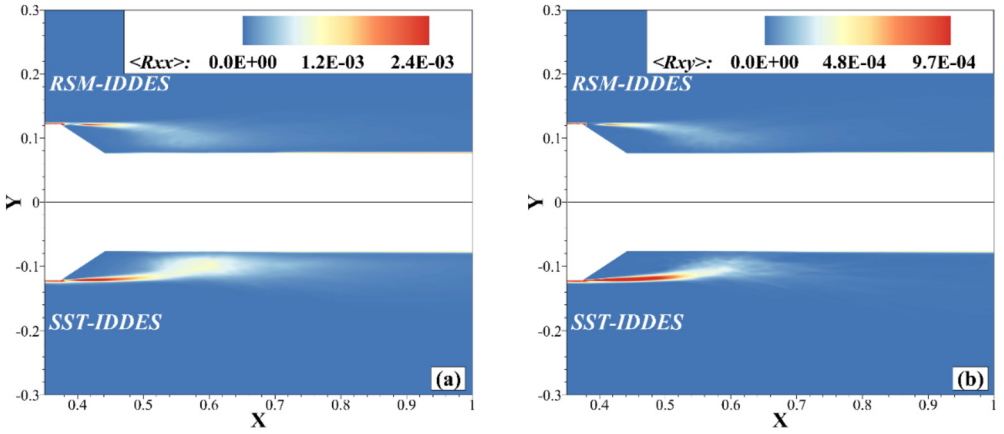


**Fig. 13.** a: Mean subgrid normal stress contour obtained from SST-IDDES and RSM-IDDES; b: Mean subgrid shear stress contour obtained from SST-IDDES and RSM-IDDES.

represents the shear layers shedding from fairing, it can be seen the "averaged" shear layer predicted by RSM-IDDES is also shorter than that of SST-IDDES. That means the instability of the shear layer by the RSM-IDDES occurs earlier than that of SST-IDDES under the mean sense. It leads the free shear layer to shorten and hit the wall earlier forming a smaller separation bubble, the evidence is also shown in Fig. 9a. On the other hand, considering the peak of $Cp_{rms}$, the simulation results of both two models are larger than the experimental data. One reason for this difference could be due to the experiment not taking the measurement at the peak position, near x=0.58), yet the result by RSM-IDDES model is smaller and closer to the experimental data than SST-IDDES model.

To compare the turbulent flow field simulated by SST-IDDES and RSM-IDDES in more detail, the time sequences of the flow field along the streamwise direction and azimuthal direction are extracted as shown in Fig. 14a. Fig. 14b shows the proportion of resolved turbulent kinetic energy to the overall turbulent kinetic energy, the resolved TKE are extracted from the line. It can be seen that both models have resolved more than 80% of the TKE, which means the grid size reaches the requirements of DES simulation for resolving the TKE [58]. The following will analyze the resolved turbulence structure by the two models from the perspective of two distributions in time and space. The analyses of power spectral density (PSD) of fluctuation velocity and turbulent kinetic energy spectrum, which respectively reflect the distribution of turbulent kinetic energy with frequency (temporal mode of Fourier analysis) at a specific position and with wavenumber (spatial mode of

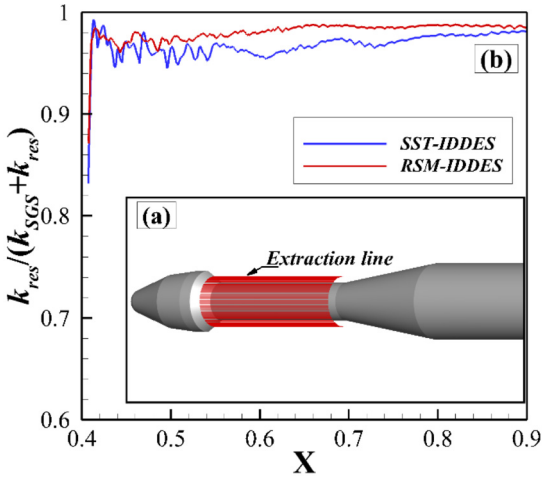


**Fig. 14.** a: Schematic diagram of extraction line distribution for Fourier analysis; b: The proportion of computed resolved turbulent kinetic energy to the overall turbulent kinetic energy obtained from SST-IDDES and RSM-IDDES along the extraction line.

Fourier analysis) at a specific moment. Since the main flow of the hammerhead configuration is axial direction flow, only the axial fluctuation velocity 'u' is considered for Fourier analysis, and the azimuthal average of the spectrum is implemented to make the spectral curves smooth. The two spectra in Fig. 15 and Fig. 16a are

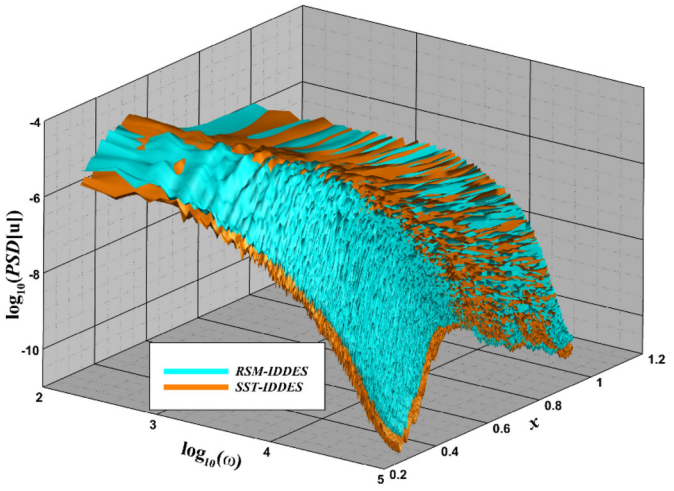


**Fig. 15.** Distribution diagram of fluctuating velocity power spectral density along the streamline direction obtained by SST-IDDES and RSM-IDDES (angular frequency and power spectral density are both logarithmic coordinates).

PSD of fluctuation velocity at each axial position and turbulent kinetic energy spectrum at each moment, respectively. The spectrum is calculated by 2600 points, which is evenly located in range of 0.412 to 0.95. All spectra are applied to the temporal or spatial sampling frequency to normalize the two-type spectra so that the integral of them at each streamwise position or moment is equal to the temporal or spatial average of resolved turbulent kinetic energy. Then these could be used to analyze the resolved turbulent kinetic energy distributions in the temporal and spatial modal.

First, from the perspective of temporal modal analysis, it can be seen from Fig. 15 that the frequency distribution of resolved turbulent kinetic energy at each axial position is a wide-frequency distribution with no dominant frequency. There are more medium and low frequency components and fewer high frequency components, which agree with the calculation in Ref. [20] and experiment in Ref. [55]. In the medium and low frequency ranges (angular frequency is lower than $10^4$), in front of the free shear layer attachment point, the amplitude of fluctuation velocity PSD gradually increases and reaches the peak near the attached point (near x=0.6). Behind the attached point, the amplitude of PSD mostly remains constant after a short period of decrease. In the high frequency range, the amplitude of PSD gradually decreases as the flow develops backward along the axial direction after the attached point. This is due to the dissipation of high-frequency turbulent kinetic energy. From the comparison of fluctuation velocity PSD simulated by the two methods in Fig. 15, the RSM-IDDES method can capture more turbulent fluctuation (the amplitude of RSM-IDDES is larger than SST-IDDES) in the separation bubble, especially in the middle and high frequency regions, and there are few differences between the two methods outside the separation bubble.

On the other hand, from the perspective of spatial modal analysis, it can be seen from Fig. 16a that the distribution of resolved turbulent kinetic energy in the spatial wavenumber at each specific moment presents a classical distribution. This has low wavenumber turbulent kinetic energy component than medium and high wavenumber, and the turbulent kinetic energy component gradually decreases as the wavenumber increases. The variation of the turbulent kinetic energy spectrum in the time history is different from the variation of fluctuation velocity PSD in the spatial range. The turbulent kinetic energy spectrum slightly fluctuates around the mean energy spectrum (as shown in Fig. 16b) over the whole time history since the fluctuation velocity is close to a stationary random process with a mean value of 0. The slight fluctuation of the turbulent kinetic energy spectrum in time history is due to the variations of turbulent flow field structures at each time caused by the development of the free shear layer. Comparing the simulation results of SST-IDDES and RSM-IDDES, the low wavenumber components of the turbulent kinetic energy spectrum of the two methods are almost the same, while the medium and high wavenumber components obtained by RSM-IDDES are relatively more than SST-IDDES. The more high-wavenumber turbulent kinetic energy components are captured by RSM-IDDES, means that the finer turbulent structures are simulated. The same is also reflected in the turbulent eddy structure depicted by the density gradient contour in Fig. 9a. To visualize this difference between the two methods more clearly, the energy spectrum is averaged over the time distribution as shown in Fig. 16b. The Kolmogorov law (with a k−5/3 slope) is observed. It is worth noting that the spectrum predicted by RSM-IDDES method has a greater subrange that follows the Kolmogorov law.

## 4. Conclusion

A general construction approach of a class of DES methods, which have the turbulent length-scale equation, is presented based on the assumption of equilibrium turbulence. By using the proposed construction approach, an IDDES method based on SSG/LRR-$\omega$ RSM turbulent model has been developed and implemented in an in-house hybrid unstructured Navier-Stokes solver. The model coefficients of the RSM-based IDDES method are calibrated by DIT simulations. The performance of RSM-IDDES has been explored by simulating the massively separated flows around the tandem cylinders and the transonic buffet flow over a hammerhead launch vehicle. The predictions are validated by the available experimental data, and the performance is evaluated by means of instantaneous, statistical, spectral analysis of the numerical data comparing with that of SST-based IDDES. The result indicates that the mean $Cp$ and $Cp_{rms}$ obtained by the RSM-based IDDES method show better agreements with the experiments than that of SST-based IDDES.

The massively separated flow behind the bluff body is well reproduced. The flow topology is characterized by the free shear layer developing from the upstream boundary layer and gradually losing stability after a period of extension. After the free shear layer loses stability, it breaks into various scales vortices and merges together as they are being convected downstream and forms the wake. These processes that result from the anisotropy in the Reynolds stress are well captured by the RSM-based IDDES, because the exact production terms. Thus, the RSM-based IDDES provides more refined vortex structures than the SST-IDDES method and shows a certain advantage over the SST-based IDDES method, as compared with experiments.

Work is currently under way to study the buffet flow around NASA common research model, as well as to improve the performance of RSM-IDDES.

## Declaration of competing interest

The authors declare there are no conflicts of interest regarding the publication of this paper.

## Acknowledgements

The research was supported by National Natural Science Foundation of China (No. 92052109, No. 12102439 and No. 11772265) and the “111” Project of China (No. B17037). The authors thankfully acknowledge these institutions.

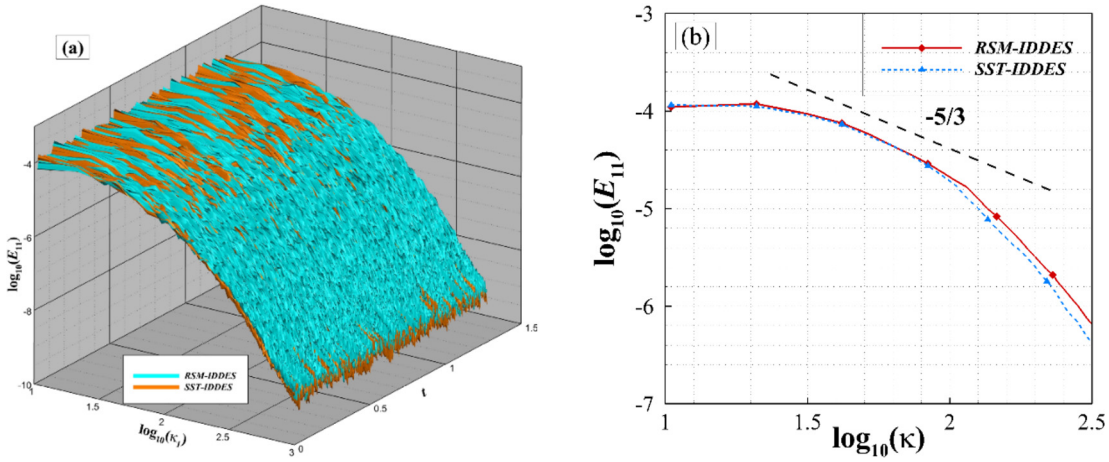


**Fig. 16.** a: Distribution diagram of fluctuating velocity energy spectrum along the time history obtained by SST-IDDES and RSM-IDDES (angular wavenumber and energy spectrum are both logarithmic coordinates); b: Distribution diagram of fluctuating velocity energy spectrum with the time average obtained from SST-IDDES and RSM-IDDES (angular wavenumber and energy spectrum are both logarithmic coordinates).

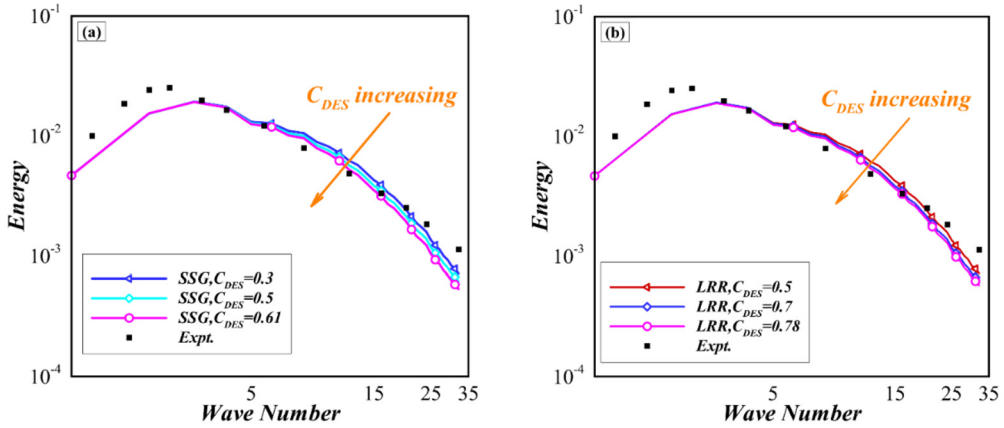


**Fig. B1.** Effect of different $C_{DES}$-constants in RSM-IDDES on the energy spectrum in the DIT case, $t^* = 2.0$ (a. SSG branch, b. LRR branch).

## Appendix A. Adaptive dissipation Roe scheme

The adaptive dissipation Roe scheme [39,40] is given by:

$$\boldsymbol{F}_{adapt} = \frac{1}{2}(\boldsymbol{F}_L + \boldsymbol{F}_R) - \phi\frac{1}{2}|\mathbf{A}_{Roe}|(\boldsymbol{Q}_R - \boldsymbol{Q}_L) \tag{A.1}$$

$\boldsymbol{F}_L, \boldsymbol{F}_R$ are the left and right values of the convective flux respectively. $\mathbf{A}_{Roe}$ is the Roe matrix. $\boldsymbol{Q}_R, \boldsymbol{Q}_L$ are the left and right values of conserved variable respectively. $\phi$ is the adaptive dissipation factor.

$$\phi = \phi_{\max}\tanh\left(A^{CH1}\right) \tag{A.2}$$

Where $A = CH2 \cdot \max\{[C_{DES}\Delta/L_{turb}/g - 0.5]; 0\}$, $L_{turb} = [(\upsilon_t + \upsilon)/(C_\mu^{3/2}K)]^{1/2}$, $K = \max\{[(S^2 + \Omega^2)/2]^{1/2}; 0.1\tau^{-1}\}$.
$\tau$ is the characteristic time which is calculated by characteristic length and velocity ($\tau = L_0/U_0$), $g = \tanh(B^4)$ and $B = CH3 \cdot \Omega \cdot \max(\Omega, S)/\max[(S^2 + \Omega^2)/2, 10^{-20}]$, $S = \sqrt{2\tilde{S}_{ij}\tilde{S}_{ij}}$, $\Omega = \sqrt{2\tilde{W}_{ij}\tilde{W}_{ij}}$, $\widetilde{W}_{ij} = (\tilde{U}_{i,j} - \tilde{U}_{j,i})/2$.
The constants are given as: $\phi_{\max} = 1$, $CH1 = 3$, $CH2 = 1$, $CH3 = 2$.

## Appendix B. Calibration of $C_{DES}$ using Roe scheme

The numerical dissipation has a significant influence on the energy spectrum of DIT, as presented in Ref. [39]. Therefore, the adaptive dissipation Roe scheme has been used in the whole study. The $C_{DES}$ is a parameter that is also occupied in the scheme, and the value of $C_{DES}$ will affect the numerical dissipation. In order to validate the RSM-IDDES in our code, we have also performed the DIT simulations with the Roe scheme. The numerical dissipation is manually reduced by using a very small dissipation factor ($\phi = 0.05$). The results are plotted in Fig. B1. It was found that $C_{DES,LRR} = 0.5$ and $C_{DES,SSG} = 0.3$ show better performance at the high-wavenumber.

## References

[1] Haecheon Choi, Woo-Pyung Jeon, Jinsung Kim, Control of flow over a bluff body, Annu. Rev. Fluid Mech. 40 (2008) 113–139, https://doi.org/10.1146/annurev.fluid.39.050905.110149.
[2] Beiji Shi, Xiaolei Yang, Guodong Jin, Guowei He, Shizhao Wang, Wall-modeling for large-eddy simulation of flows around an axisymmetric body using the diffuse-interface immersed boundary method, Appl. Math. Mech. (2019) 305–320, https://doi.org/10.1007/s10483-019-2425-6.
[3] Wenyao Cui, Jian Liu, Yuanhao Sun, Qibing Li, Zhixiang Xiao, Airbrake controls of pitching moment and pressure fluctuation for an oblique tail fighter model, Aerosp. Sci. Technol. 81 (2018) 294–305, https://doi.org/10.1016/j.ast.2018.08.016.
[4] R. Camussi, A. Di Marco, C. Stoica, M. Bernardini, F. Stella, F. De Gregorio, F. Paglia, L. Romano, D. Barbagallo, Wind tunnel measurements of the surface pressure fluctuations on the new VEGA-C space launcher, Aerosp. Sci. Technol. 99 (2020) 105772, https://doi.org/10.1016/j.ast.2020.105772.
[5] Yufei Zhang, Haixin Chen, Kan Wang, Meng Wang, Aeroacoustic prediction of a multi-element airfoil using wall-modeled large-eddy simulation, AIAA J. 55 (12) (2017) 4219–4233, https://doi.org/10.2514/1.J055853.

[6] S.S. Girimaji, E. Jeong, R. Srinivasan, Partially averaged Navier-Stokes method for turbulence: fixed point analysis and comparison with unsteady partially averaged Navier-Stokes, J. Appl. Mech. 73 (3) (2006) 422, https://doi.org/10.1115/1.2173677.
[7] Roland Schiestel, Anne Dejoan, Towards a new partially integrated transport model for coarse grid and unsteady turbulent flow simulations, Theor. Comput. Fluid Dyn. 18 (6) (2005) 443–468.
[8] Philippe R. Spalart, Comments on the feasibility of LES for wings, and on a hybrid RANS/LES approach, in: Proceedings of First AFOSR International Conference on DNS/LES, Greyden Press, 1997.
[9] Sébastien Deck, Numerical simulation of transonic buffet over a supercritical airfoil, AIAA J. 43 (7) (2005) 1556–1566, https://doi.org/10.2514/1.9885.
[10] Stefan Heinz, A review of hybrid RANS-LES methods for turbulent flows: concepts and applications, Prog. Aerosp. Sci. 114 (2020) 100597, https://doi.org/10.1016/j.paerosci.2019.100597.
[11] P.R. Spalart, S. Deck, M.L. Shur, K.D. Squires, M.Kh. Strelets, A. Travin, A new version of detached-eddy simulation, resistant to ambiguous grid densities, Theor. Comput. Fluid Dyn. 20 (3) (2006) 181–195, https://doi.org/10.1007/s00162-006-0015-0.
[12] M. Shur, P.R. Spalart, M. Strelets, A. Travin, A hybrid RANS/LES approach with delayed DES and wall-modelled LES capabilities, Int. J. Heat Fluid Flow 29 (6) (2008) 1638–1649, https://doi.org/10.1016/j.ijheatfluidflow.2008.07.001.
[13] J. Riou, E. Garnier, S. Deck, C. Basdevant, Improvement of delayed-detached eddy simulation applied to separated flow over missile fin, AIAA J. 47 (2) (2009) 345–360, https://doi.org/10.2514/1.37742.
[14] P.R. Spalart, Detached-eddy simulation, Annu. Rev. Fluid Mech. 41 (1) (2009) 181–202, https://doi.org/10.1146/annurev.fluid.010908.165130.
[15] M. Strelets, Detached Eddy Simulation of Massively Separated Flows, AIAA Paper 2001-0879, Jan. 2001, https://doi.org/10.2514/6.2001-879.
[16] Zhixiang Xiao, Haixin Chen, Yufei Zhang, Jingbo Huang, Song Fu, Study of delayed-detached eddy simulation with weakly nonlinear turbulence model, J. Aircr. 43 (5) (2006) 1377–1385, https://doi.org/10.2514/1.20127.
[17] Jee SolKeun, Karim Shariff, Detached-eddy simulation based on the v2-f model, Int. J. Heat Fluid Flow 46 (2014) 84–101, https://doi.org/10.1016/j.ijheatfluidflow.2013.12.006.
[18] Maochao Xiao, Yufei Zhang, Assessment of the SST-IDDES with a shear-layer-adapted subgrid length scale for attached and separated flows, Int. J. Heat Fluid Flow 85 (2020) 108653, https://doi.org/10.1016/j.ijheatfluidflow.2020.108653.
[19] Shusheng Chen, Zheng Li, Wu Yuan, HuaFeng Yu, Chao Yan, Investigations on high-fidelity low-dissipation scheme for unsteady turbulent separated flows, Aerosp. Sci. Technol. (2021) 106785, https://doi.org/10.1016/j.ast.2021.106785.
[20] Yi Liu, Gang Wang, Hongyu Zhu, Zhengyin Ye, Numerical analysis of transonic buffet flow around a hammerhead payload fairing, Aerosp. Sci. Technol. (2018), https://doi.org/10.1016/j.ast.2018.11.002.
[21] M. Mirzaei, A. Sohankar, The evaluation of a detached eddy simulation based on the $k$–$\omega$–$\overline{v^2}$–$f$ model with three flow configurations, Aerosp. Sci. Technol. 43 (2015) 199–212, https://doi.org/10.1016/j.ast.2015.03.002.
[22] Chuangxin He, Yingzheng Liu, A dynamic detached-eddy simulation model for turbulent heat transfer: impinging jet, Int. J. Heat Mass Transf. 127 (2018) 326–338, https://doi.org/10.1016/j.ijheatmasstransfer.2018.06.117.
[23] Charles Mockett, A comprehensive study of detached eddy simulation, Ph.D. thesis, Berlin, 2009.
[24] René-Daniel Cécora, Rolf Radespiel, Bernhard Eisfeld, Axel Probst, Differential Reynolds-stress modeling for aeronautics, AIAA J. 53 (3) (2015) 739–755, https://doi.org/10.2514/1.J053250.
[25] Neil Ashton, Jefferson Davis, Christoph Brehm, Assessment of the elliptic blending Reynolds stress model for a rotating turbulent pipe flow using new dns data, in: AIAA Aviation 2019 Forum, 2019.
[26] Xiaoyu Yang, Paul G. Tucker, Assessment of turbulence model performance: large streamline curvature and integral length scales, Comput. Fluids 126 (2016) 91–101, https://doi.org/10.1016/j.compfluid.2015.11.010.
[27] Matthew J. Churchfield, Gregory A. Blaisdell, Reynolds stress relaxation turbulence modeling applied to a wingtip vortex flow, AIAA J. 51 (11) (2013) 2643–2655, https://doi.org/10.2514/1.J052265.
[28] Axel Probst, Rolf Radespiel, Tobias Knopp, Detached-eddy simulation of aerodynamic flows using a Reynolds-stress background model and algebraic RANS/LES sensors, in: 20th AIAA Computational Fluid Dynamics Conference, 2011.
[29] S. Jakirlic, K. Hanjalic, A new approach to modelling near-wall turbulence energy and stress dissipation, J. Fluid Mech. 459 (2002) 139, https://doi.org/10.1017/S0022112002007905.
[30] R.N. Zhuchkov, A.A. Utkina, Combining the SSG/LRR-$\omega$ differential Reynolds stress model with the detached eddy and laminar-turbulent transition models, Fluid Dyn. 51 (6) (2016) 733–744.
[31] Mikhail L. Shur, et al., An enhanced version of DES with rapid transition from RANS to LES in separated flows, Flow Turbul. Combust. 95 (4) (2015) 709–737, https://doi.org/10.1007/s10494-015-9618-0.
[32] Bernhard Eisfeld, Olaf Brodersen, Advanced turbulence modelling and stress analysis for the DLR-F6 configuration, in: 23rd AIAA Applied Aerodynamics Conference, 2005.
[33] Julianne Dudek, Jan-Renee Carlson, Evaluation of full Reynolds stress turbulence models in fun3d, in: 55th AIAA Aerospace Sciences Meeting, 2017.
[34] Tue Nguyen, Milos Vukovic, Marek Behr, Birgit Reinartz, Numerical simulations of successive distortions in supersonic turbulent flow, AIAA J. 50 (11) (2012) 2365–2375, https://doi.org/10.2514/1.J051465.
[35] Bernhard Eisfeld, Christopher L. Rumsey, Influence of length-scale correction on predicting aeronautical flows, in: AIAA Aviation 2020 Forum, 2020.
[36] Gang Wang, Zhengyin Ye, Mixed element type unstructured grid generation and its application to viscous flow simulation, in: 24th International Congress of Aeronautical Sciences, Yokohama, Japan, 2004.
[37] Ami Harten, James M. Hyman, Self-adjusting grid methods for one-dimensional hyperbolic conservation laws, J. Comput. Phys. 50 (2) (1982) 235–269, https://doi.org/10.1016/0021-9991(83)90066-9.
[38] Timothy Barth, Dennis Jespersen, The design and application of upwind schemes on unstructured meshes, in: 27th Aerospace Sciences Meeting, 1989.
[39] Zhixiang Xiao, Jian Liu, Jingbo Huang, Song Fu, Numerical dissipation effects on massive separation around tandem cylinders, AIAA J. 50 (5) (2012) 1119–1136, https://doi.org/10.2514/1.J051299.
[40] F. Ducros, V. Ferranda, F. Nicoud, C. Weber, D. Darracq, C. Gacherieu, T. Poinsot, Large-eddy simulation of the shock/turbulence interaction, J. Comput. Phys. 152 (2) (1999) 517–549, https://doi.org/10.1006/jcph.1999.6238.
[41] Paul A. Durbin, B.A. Pettersson Reif, Statistical Theory and Modeling for Turbulent Flows, vol. 2, Wiley, Chichester, 2011.
[42] Chuangxin He, Yingzheng Liu, Savas Yavuzkurt, A dynamic delayed detached-eddy simulation model for turbulent flows, Comput. Fluids 146 (2017) 174–189, https://doi.org/10.1016/j.compfluid.2017.01.018.
[43] Florian R. Menter, Two-equation eddy-viscosity turbulence models for engineering applications, AIAA J. 32 (8) (1994) 1598–1605, https://doi.org/10.2514/3.12149.
[44] G. Comte-Bellot, S. Corrsin, Simple Eulerian time correlation of full- and narrow-band velocity signals in grid-generated 'isotropic' turbulence, J. Fluid Mech. 48 (2) (1971) 273–337, https://doi.org/10.1017/S0022112071001599.
[45] Marcel Lesieur, Turbulence in Fluids, vol. 40, Springer Science & Business Media, 2008.
[46] L.N. Jenkins, M.R. Khorrami, M.M. Choudhari, C.B. McGinley, Characterization of Unsteady Flow Structures Around Tandem Cylinders for Component Interaction Studies in Airframe Noise, AIAA Paper 2005-2812, May 2005, https://doi.org/10.2514/6.2005-2812.
[47] D.H. Neuhart, L.N. Jenkins, M.M. Choudhari, M.R. Khorrami, Measurements of the Flowfield Interaction Between Tandem Cylinders, AIAA Paper 2009-3275, May 2009, https://doi.org/10.2514/6.2009-3275.
[48] Rui Wang, Hongbo Zhu, Yan Bao, Dai Zhou, Huan Ping, Zhaolong Han, Hui Xu, Modification of three-dimensional instability in the planar shear flow around two circular cylinders in tandem, Phys. Fluids 31 (2019) 104110, https://doi.org/10.1063/1.5120564.
[49] Guillaume A. Brès, David Freed, Michael Wessels, Swen Noelting, Franck Pérot, Flow and noise predictions for the tandem cylinder aeroacoustic benchmark, Phys. Fluids 24 (3) (2012) 036101, https://doi.org/10.1063/1.3685102.
[50] Yuji Tasaka, Seiji Kon, Lionel Schouveiler, Patrice Le Gal, Hysteretic mode exchange in the wake of two circular cylinders in tandem, Phys. Fluids 18 (8) (2006) 084104, https://doi.org/10.1063/1.2227045.
[51] http://cfd.mace.manchester.ac.uk/ATAAC/WebHome [retrieved 2019].
[52] A. Garbaruk, M. Shur, M. Strelets, P.R. Spalart, R. Balakrishnan, DDES and IDDES of tandem cylinders, No. ANL-10/26, Argonne National Lab. (ANL), Argonne, IL, United States, 2010.
[53] Eduardo Molina, Beckett Y. Zhou, Juan J. Alonso, Marcello Righi, Roberto G. Silva, Flow and noise predictions around tandem cylinders using DDES approach with SU2, in: AIAA Scitech 2019 Forum, 2019.
[54] Björn Greschner, Dandy Eschricht, Charles Mockett, F. Thiele, Turbulence modelling effects on tandem cylinder interaction flow and analysis of installation effects on broadband noise using chimera technique, in: 30th AIAA Applied Aerodynamics Conference, 2012.
[55] C. Coe, J. Nute, Steady and Fluctuating Pressures at Transonic Speeds on Hammerhead Launch Vehicles, NASA TMX-778, December 1962.
[56] R.M. Cummings, S.A. Morton, D.R. Mcdaniel, Experiences in accurately predicting time-dependent flows, Prog. Aerosp. Sci. 44 (4) (2008) 241–257, https://doi.org/10.1016/j.paerosci.2008.01.001.
[57] Grégoire Pont, Paola Cinnella, Jean-Christophe Robinet, Pierre Brenner, Assessment of automatic hybrid RANS/LES models for industrial CFD, in: 32nd AIAA Applied Aerodynamics Conference, 2014.
[58] Stephen B. Pope, Turbulent Flows, 2000, pp. 558–561.